MICROSENSOR MODELING

H. P. Baltes*, W. Allegretto**, A. Nathan***

*Physical Electronics Laboratory, Institute of Quantum Electronics,
Swiss Federal Institute of Technology (ETH), Zürich, Switzerland

**Department of Mathematics, University of Alberta, Edmonton, Canada

***Research and Development, LSI Logic Corporation, Santa Clara, USA

SUMMARY

Sensors convert physical or chemical measurands into electronic signals.
Microsensors are manufactured using microelectronic processing technologies.
The goal is to develop batch-fabricated sensors interfaced with microprocessors or
application specific integrated circuits. Device modeling is becoming an essential tool
for microsensor design and analysis. This new field of microsensor modeling is
reviewed in this paper. Model equations and boundary conditions are presented along
with numerical procedures and selected results.

INTRODUCTION

A sensor or "entrance transducer" is a device which converts a physical or
chemical signal into an electronic signal that can be readily processed, stored, or
transmitted. Sensors are required at the front end of measurement and control
systems or robots. Microsensors or integrated sensors can be designed and
manufactured using standard silicon integrated circuit (IC) technologies such as CMOS
or bipolar technology with or without additional sensor-specific processing steps. The
use of IC technology offers the advantage of integrating the sensing elements with
support and signal conditioning circuitry on the same chip. Silicon has
revolutionized electronics and is now altering our perceptions of sensors as well.

Microsensors can be classified by measurands, i.e. input signals to be converted,
namely magnetic, chemical, radiant, mechanical, and thermal signals. A number of
magnetic field, optical, pressure, and temperature microsensors has been achieved in
standard silicon IC technology by inventive device designs without requiring any
special processing steps. Examples are integrated Hall sensors, magnetotransistors,
photodetectors, and transistor-based pressure and temperature sensors. Other sensors,
notably chemical and mechanical sensors, require dedicated post-processing steps
such as the deposition of specific films or the creation of geometric structures by
microlithography and etching (micromachining). Examples are capacitive humidity
sensors with water adsorbing layer, chemical sensors made selective by applying an
enzyme layer catalyzing the reaction of one specific compound, and various
mechanical sensors based on silicon microstructures produced by etching, such as
microbridges, diaphragms, and cantilever beams.

Timely information on the rapidly growing field of microsensor research can be
found in recent reviews [1,2], conference proceedings [3,4], special journal issues [5],
and in the dedicated journals "Sensors and Actuators" and "Sensors and Materials". The
wealth of approaches, methods, and tools can be classified in the four broad categories

of (i) silicon IC technology (standard fabrication process, but dedicated device design and test of sensor functions), (ii) film deposition, (iii) micromachining, and (iv) device modeling. The last mentioned area of microsensor modeling is the topic of this paper.

The modeling of semiconductor IC devices is a highly developed art, as is manifested by the many contributions to this volume. In contrast, the field of microsensor modeling is still in its infancy. The motivation behind IC device modeling -- reduction of the number of costly trial-and-error fabrication cycles and insight in the physical properties of the device interior not readily accessible by experiment -- is even more compelling in the case of microsensors. The goal is to understand the sensor's operating principles and, in particular, how design, fabrication, and operating parameters determine, enhance, or limit its sensitivity with respect to the measurand under consideration.

By design, the presence of the physical or chemical input signal is meant to "upset" an "ordinary" IC device as much as possible, which makes the device modeling task even more difficult. For example, magnetic induction disturbs the carrier transport by the Lorentz force; incident radiation alters the generation recombination balance in photodetectors; mechanical stress can modulate the electric conductivity. The measurand often appears in the form of an external field that reduces the symmetry of the device operation, hence making the choice of appropriate model equations, physical and material parameters, as well as boundary and interface conditions very crucial.

Simple analytical models of microsensor operation are useful heuristic tools for trial device design, but often may turn out to be correct, only under very special geometry and operating conditions. Numerical microsensor modeling is indispensable for analysing general and more complex situations. Solar cells and photodiodes are probably the best understood semiconductor sensors and the latter can often be treated adequately by one-dimensional numerical modeling. A variety of one and two dimensional numerical codes have been developed (see [6] and [7]) that solve the drift-diffusion based system of equations in the presence of optical radiation. In view of the vector character of magnetic induction, at least two-dimensional modeling is usually required for magnetic sensors [8]. For these problems, we have developed ALBERTINA- a package that provides numerical solutions to the system of equations governing carrier transport in Hall type [9] and bipolar magnetic field sensors [10,11]. As far as pressure sensors are concerned, we are only aware of SENSIM [12] and ANSYS (see [13]), that can provide a full numerical analysis of the interactions of mechanical, thermal, and electrical effects in such devices.

MODELING EQUATIONS

The fundamental system of partial differential equations that describe the physical processes occuring in integrated sensors, are usually given in the following macroscopic form

$$\text{div}\,(\varepsilon E) = \rho$$

$$\text{div}\,J_n - q\,\partial n/\partial t = q\,(R - G) \qquad (1)$$

$$\text{div}\,J_p + q\,\partial p/\partial t = -\,q\,(R - G),$$

in the usual notation (see [14]). Although the equations are a result of many approximations [14], they are nevertheless justified in view of the physical dimensions and operating conditions normally encountered in practical sensing structures. Depending on the nature of the measurand, the various quantities in system (1) have to be suitably modeled to account for the variety of physical effects (and their interactions) taking place in the device. Some of the pertinent models are described in what follows.

Temperature effects

Semiconductor devices are sensitive to variations in temperature, whether applied externally or generated within the device. A variety of methods are possible for utilising devices and circuits in standard IC technology, as temperature transducers. A review of temperature transducers can be found in [15]. To allow for the effects of temperature, the transport relations for J_n and J_p in system (1), for not too large temperature gradients are [14]

$$J_n = -qD_n\,(T)\,[\text{grad } n - n\,\text{grad }(q\psi/kT)] + qnD_n^{\,T}(T)\,\text{grad } T \qquad (2)$$

$$J_p = -qD_p\,(T)\,[\text{grad } p + p\,\text{grad }(q\psi/kT)] - qpD_p^{\,T}\,(T)\,\text{grad } T, \qquad (3)$$

including a component of electric current density with the temperature gradient as a driving force. The temperature dependent concentration diffusion constants, $D_{n,p}$ and the drift mobilities, $\mu_{n,p}$ are assumed to be related by Einstein's relations and the thermal diffusion constants, $D_{n,p}$ can be assumed equal to $D_{n,p}(T)/2T$ (see [14]). The carrier concentrations n and p are assumed to follow Maxwell-Boltzmann statistics,

$$n = n_{ie}\,\exp\,[(\psi - \varphi_n)/V_t] \qquad (4)$$

$$p = n_{ie}\,\exp\,[(\varphi_p - \psi)/V_t], \qquad (5)$$

where V_t denotes the thermal voltage, n_{ie} the effective intrinsic concentration, and $\varphi_{n,p}$ denote the respective Fermi potentials. An elaborate account of the temperature dependence of the various terms in (1) to (3) can be found in [14,16]. The models are identical to those used in IC device modeling. Electrical and thermal interactions in the device can be accounted for by an additional heat flow equation, viz.,

$$\text{div }[\kappa(T)\,\text{grad } T] = \rho c\,\partial T/\partial t - H \qquad (6)$$

with $\kappa(T)$ denoting the thermal conductivity, ρ the mass density and c the specific heat. H accounts for the various heat sources and sinks in the system. Equations (1) to (6) adequately describe the thermoelectric effects and in particular the Seebeck effect which can be exploited in thermal sensing [17].

Optical radiation

Physical processes in optoelectronic devices such as photodiodes and solar cells can be described by (1) to (3), but optical generation of carriers has to be taken into account. For monochromatic radiation with zero reflectance at the diode back surface, optical generation at depth x into the device can be generally expressed as [6,7]

$$G(x) = \int_{0}^{\infty} (1 - \Gamma)\, \varphi\, \alpha\, e^{-\alpha x}\, d\lambda, \tag{7}$$

where φ is the incident photon flux per unit area normal to the device, Γ the front surface reflection coefficient, α is the absorption coefficient, all being functions of the wavelength, λ. For multiple reflections between front and back surfaces, the integrand in (7) becomes more complicated (see [7]). In avalanche photodiodes, the high reverse bias voltage across the depletion zone leads to e-h pair generation from high energy electrons and holes in the depletion region, thus requiring the inclusion of impact ionisation in the continuity equations. High doping effects particularly in solar cells result in the recombination term, R accounting for both Auger and Shockley- Read- Hall processes. The dependence of the intrinsic carrier concentration and carrier lifetimes, $\tau_{n,p}$ on doping concentration are modified accordingly [14,16]. Also the electric potential in the current density relations in (2) and (3), have to be replaced by effective potentials accounting for variations in band structure and the Fermi-Dirac statistics (see [18]).

As for the boundary conditions, the electric potential and carrier densities at ohmic contacts (assumed ideal) are prescribed by the usual Dirichlet conditions [14],

$$\psi = V_a + (kT/q) \sinh^{-1} (N/2n_i)$$

$$n = (N^2/4 + n_i^2)^{1/2} + N/2 \tag{8}$$

$$p = (N^2/4 + n_i^2)^{1/2} - N/2,$$

where N denotes the net ionised impurity concentration. We note that relations (8), hold for the various other sensors whose output is electrical. At the interface between two different media, the net electric displacement normal to the interface is assumed equal to the interface charge density. The current densities at insulating boundaries is determined by the recombination at the interface [6], for nonideal interfaces.

Magnetic field effect

In the presence of a magnetic field, the action of the Lorentz force on moving carriers manifests itself in the transport equations. Under various assumptions [19], the magnetic field dependent electric current densities can be expressed in the classical drift-diffusion formulation as

$$J_{nB} + \mu_n^* J_{nB} \times B = qD_n\, [\mathrm{grad}\, n - n\, \mathrm{grad}\, (q\psi/kT)] \tag{9}$$

$$J_{pB} - \mu_p^* J_{nB} \times B = -qD_p\, [\mathrm{grad}\, p + p\, \mathrm{grad}\, (q\psi/kT)]. \tag{10}$$

The transport relations are a good approximation only in the weak field limit, $(\mu_{n,p}^{*}B)^2$ << 1, with a relative error that is of the order of $(\mu_{n,p}^{*}B)^2$. The equations take into account the direct effects of temperature on the various coefficients, but they do not include thermoelectric and thermomagnetic effects. The Hall mobility, μ_n^{*} is assumed proportional to the drift mobility, μ_n with the constant of proportionality being the Hall scattering coefficient. The experimental value of this coefficient has been found to be significantly different from theory, particularly in the limit of ionised impurity scattering [20]. In general, this coefficient depends on the nature of the scattering mechanism, the band structure, the degree of degeneracy, and on the statistics characterising the velocity distribution of carriers [21]. In view of the scattering mechanisms normally assumed in the simulations, and in weak magnetic fields, a value of 1.2 for the scattering coefficient for both electrons and holes [11] can be adopted.

System (1) together with relations (9) and (10) are solved subject to a mixture of Dirichlet and homogeneous Neumann boundary conditions. At ohmic contacts (assumed ideal), the electrostatic potential and carrier concentrations at the contact are prescribed by the usual Dirichlet boundary conditions (8). At insulating boundaries, the presence of a magnetic field could result in a significant Hall field at the boundaries. In such a case, the standard condition grad ψ . n = 0 at these insulating boundaries may be physically invalid (n denotes the outward normal vector) and therefore, the procedure introduced in [10] is adopted. The actual boundary condition on ψ at these boundaries is treated as unknown and to deal with the problem an "artificial" oxide region is introduced, which completely encloses the device domain. In this way, one avoids imposing artificial boundary conditions at the device/oxide interface which could a priori affect the results. The discontinuities in the normal component of electric field at the interface are handled in the weak formulation of the equations. Poisson's equation is solved over the entire domain (consisting of the device plus oxide), with the normal component of electric field taken to be zero at the oxide's outer edges. The nature of this condition could, in principle, affect the solution in the device's active region. These effects, however, can be made minimal by an appropriate choice of the oxide thickness. The solutions of the continuity equations are restricted to the device domain. At the semiconductor/oxide interface, the zero normal current condition J_n . $n = J_p$. n = 0 is imposed for ideal interfaces.

Mechanical effects

The effect of mechanical stress in a p-n junction can be exploited in realising bipolar transistors whose output characteristics are a function of the applied stress [22,23]. Stress-induced variations in the energy band structure affect the intrinsic concentration which then becomes

$$n_{i\sigma}^{2} = n_{ie}^{2} \exp\left[\alpha P/kT\right], \tag{11}$$

where α is 10^{-5} eV/bar for a uniaxial stress in the <100> direction and P denotes the applied pressure (see [23]). Consequently, the majority and minority carrier concentrations in the base region are affected. The stress also induces a change in the carrier mobility. The change in mobility, $\Delta\mu$ is linearly related to the stress,

$$\Delta\mu = -\mu\sigma\delta, \tag{12}$$

where $\delta = 10^{-4}$ bar^{-1} and σ denotes the stress. There is also a change in the free carrier lifetime due to the stress induced generation-recombination centres.

Mechanical Equations and Boundary Conditions

The basic effects exploited by pressure sensors are piezoelectric, piezoresistive, or capacitive. The effects most commonly utilised by integrated Si pressure sensors are piezoresistive (ΔR) or capacitive (ΔC) which are inherent in a thin diaphragm. Based on the approximations employed in the thermoelastic plane-stress formulation [24], the equations governing stress, F and deflection, ω in a diaphragm are given by:

$$\partial^2/\partial y^2 \; [1/E \; (\partial^2 F/\partial y^2 - v\partial^2 F/\partial x^2)] + 2\partial^2/\partial x\partial y \; [1/G \; (\partial^2 F/\partial x\partial y)]$$

$$+ \; \partial^2/\partial x^2 \; [1/E \; (\partial^2 F/\partial x^2 - v\partial^2 F/\partial y^2)]$$

$$= -(1-v) \; [\partial^2/\partial x^2(N_T/E) + \partial^2/\partial y^2(N_T/E)], \tag{13}$$

$$\partial^2/\partial x^2 \; [D_1 \; \partial^2\omega/\partial x^2 + D_2 \; \partial^2\omega/\partial y^2)] + 2\partial^2/\partial x\partial y \; [D_3 \; \partial^2\omega/\partial x\partial y]$$

$$+ \; \partial^2/\partial y^2 \; [D_2 \; \partial^2\omega/\partial x^2 + D_1 \; \partial^2\omega/\partial y^2)]$$

$$= q - [1/(1-v)] \; [\partial^2 M_T/\partial x^2 - \partial^2 M_T/\partial y^2]. \tag{14}$$

In eqns. (13) and (14), E denotes the effective Young's modulus, G the effective shear modulus, N_T the thermal load, M_T the thermal bending moment, q is the effective loading, v denotes Poisson's ratio, F the stress function, and ω the diaphragm deflection. $D_1, D_2, D_3,$ and M_T are assumed constants and are given in [24]. The boundary conditions for (13) are as follows,

$$\partial^2 F/\partial x^2 = N_s \; \text{ and } \; \partial^2 F/\partial x\partial y = 0 \qquad \text{for } y = \pm \, L/2,$$

$$\partial^2 F/\partial y^2 = N_s \; \text{ and } \; \partial^2 F/\partial x\partial y = 0 \qquad \text{for } x = \pm \, L/2, \tag{15}$$

where N_s is a surface traction force caused by thermal mismatch between the silicon substrate and packaging/mounting material and/or external forces, and L is the diaphragm side dimension (Fig. 1). The boundary conditions for (14) are [24]

$$\omega = 0 \qquad\qquad\qquad \text{at } x = \pm(L/2) \text{ or } y = \pm \, (L/2),$$

$$\partial\omega/\partial x = gM_x \qquad\qquad \text{at } x = \pm \, L/2, \tag{16}$$

$$\partial\omega/\partial y = gM_y \qquad\qquad \text{at } y = \pm \, L/2,$$

where M_x and M_y are bending moments and g is the edge factor (see [24]) which is constant. Equations (13) and (14) solved with boundary conditions (15) and (16) yield the stress components, σ_{xx}, σ_{yy}, and σ_{xy} in the diaphram. In the case of bridge and cantilever structures, the boundary conditions (15) and (16) become suitably modified.

For piezoresistive pressure transducers, the fractional change of resistivity $\delta\rho$ as a result of stress σ is [24],

$$\delta\rho_i = \sum_{j=1}^{6} \pi_{ij}\,\sigma_j \qquad (17)$$

where i (=1,2,..,6) and j carry the notation such that $xx \Rightarrow 1$, $yy \Rightarrow 2$, $zz \Rightarrow 3$, $yz \Rightarrow 4$, $xz \Rightarrow 5$, and $xy \Rightarrow 6$. For a diaphragm in x-y plane, employing the plane stress approximation (σ_{xz}, σ_{yz}, and σ_{zz} assumed negligible), yields the fractional change of resistance as

$$\Delta R/R_o = \pi_1\,\sigma_1 + \pi_t\,\sigma_t + \pi_{16}\,\sigma_{xy}, \qquad (18)$$

where R_o is the unstressed resistance, ΔR denotes resistance change, σ_1 is the average normal stress parallel to the current path, σ_t is the average transverse stress perpendicular to the current path, σ_{xy} is the average shear stress and $\pi_{1,t,16}$ denote the longitudinal, transverse, and shear piezoresistive coefficients.

For capacitive pressure transducers, the total effective capacitance between the diaphragm and the reference plate is given by [24],

$$C = \varepsilon_0/s^2 \iint [1 - \omega(x,y)]\,\partial x \partial y + C_p \qquad (19)$$

where C_p is the parasitic capacitance, s is the zero pressure separation between diaphragm and reference plate, and ε_0 is the dielectric constant in the cavity. The relative change of capacitance due to deflection $(C - C_o)/C$ can then be evaluated with the zero pressure capacitance C_o being $\varepsilon_o L^2/s$.

NUMERICAL PROCEDURES

Except in very special circumstances, none of the above systems of equations can be solved analytically. Consequently, a variety of numerical schemes have been introduced to obtain reasonably accurate solutions to the problems considered. For the devices we have selected, finite element/box type procedures are preferable. This approach allows flexibility in node position and density, and ease of specification of natural boundary conditions. Consequently, changes in device geometry and parameters can be easily implemented. Finite difference solvers can also be used [14,25], so the choice is based on individual preference and needs.

The first - and most important - step is the generation of a suitable grid. Our ALBERTINA grid generator consists of a hybrid scheme which combines procedures

introduced in [26,27] with a simpler generator (see Fig. 2). Roughly speaking, it works as follows [28]: given a simulation region, we first decompose the domain into subregions whose area depends on the local changes and size of the physical parameters. Each subregion is then automatically decomposed into either right angle or equilateral triangles (see Figs. 2 and 3), with element matching at the interfaces. We observe that perpendicular bisectors of the sides of such triangles must intersect within the triangle. It is easy for us to control the smallest angle in the right angled triangles thus facilitating the control of discretisation error [29,30]. Division into equilateral triangles requires relatively many nodes and is used in regions where conditions and variables are changing rapidly along curves. Division into right angle triangles uses fewer nodes and is suited to regions of slow change or of change only in one direction. This is important in view of the large physical dimensions that sensors have in general. Finally, various residues and relative changes are monitored as the solution procedure progresses. If such quantities are deemed unsatisfactory at any node(s), then the solution procedure is stopped, the grid in regions adjacent to such places is refined and the solution procedure is then resumed.

We can solve linear and nonlinear Poisson's equation, electron continuity equation, hole continuity equation, and the heat flow equation. Depending on the problem posed, an appropriate combination of the above equations is used. We briefly describe our procedure in the solution of Poisson's and the continuity equations for the case of magnetic field sensor simulations. Given ψ_0, n_0, and p_0, we solve the nonlinear potential equation for ψ_1 using a modified Newton method. Speed of convergence is improved by accelerating algorithms [31]. Since the magnetic field B does not enter in this equation, our procedure is essentially as in [14,25]. Given ψ_1, n_0, p_0, we next discretise

$$\operatorname{div}(A\,\boldsymbol{J_n}) = R\,(n,p), \tag{20}$$

where A is a nonsymmetric matrix whose entries depend on B [32]. This is done by following the averaging ideas of the Scharfetter-Gummel scheme [33] in discretising $\boldsymbol{J_n}$ in any element. A cell is constructed surrounding any node by means of perpendicular bisectors of the element sides, and Gauss's theorem is then employed to integrate (20). Observe that the presence of nonsymmetric A leads to changes in the calculations relative to the usual procedure. We next proceed to calculate p_1 by a similar procedure. We have found it advantageous to solve for self consistent n_1, p_1 before returning to calculate ψ_2. The procedure continues until self consistent values are found for ψ, n, and p. The stopping criteria used are of the order of 10^{-3} to 10^{-6} depending on the problem considered [11].

The above procedures are usually started at equilibrium. Applied bias is increased in small steps to the desired value with ψ, n, and p updated at each stage by extrapolation from the two previous values. As is well known, the above procedure works well for small R, but difficulties are encountered otherwise. In such cases, a Newtonian scheme may be applied to all variables simultaneously at the price of increased computational complexity. The above procedures lead to the inversion of numerous nonsymmetric large sparse matrices. Up to about 3000 nodes, we have observed that the package SPARSPAK [34] of direct solvers performs very well. As the number of nodes increases, however, the storage requirements become excessive. We have developed generalised preconditioned conjugate gradient procedures to handle

such problems; work in this area is still in progress.

The above discretisation ideas fail *a priori* for sensors which lead to fourth order differential equations such as those governing the mechanical behaviour of microstructures. For problems of this nature, a finite element scheme based on macrotriangles [29] is preferable. The procedure maintains the flexibility with which general micromechanical structures and geometries can be handled. For a variety of reasons, it is desirable to have apertures (holes) distributed on structures such as diaphragms and bridges. Furthermore, the boundary conditions as well as any material inhomogeneties can be handled naturally in the weak formulation of the equations. Work along these lines is currently being pursued.

Finally, we briefly describe our error checking routines. New codes are first run on simple problems whose answer is known analytically or on problems whose answer had been previously established. Current balance checks are also performed. Such steps are taken to remove obvious errors. For new problems, however, the key mathematical question is how to determine practically a suitable size for the triangles used in any subregion. Our grid generator attempts to choose this size so as to reasonably distribute the error, although we have been usually unable to obtain precise practical estimates. Moreover, errors may lie in reducing the physical device operation to a mathematical model. If such errors are large, no adjusting of triangles will suffice. In summary, the ultimate error check is based on comparison of the numerical results to the experimental results obtained for a device of similar type. This, we have strived to do as much as possible (see [9,11]).

RESULTS AND DISCUSSION

Photodiodes have the unique feature in that carrier transport analysis can be adequately treated in one dimension. Examples of numerical results in photodiodes using the one-dimensional PC-1D simulator are illustrated in Fig. 4. The simulator runs on IBM XT compatible computers and provides to the user, a variety of sophisticated physical models for both Si and GaAs photodiodes, and also allows provision for user input models. The electric field and carrier concentrations at equilibrium are illustrated in Fig. 4 for the Hamamatsu 1337 photodiode using the default parameters in PC-1D. The limitations of PC-1D, particularly in simulating the short circuit photocurrent in high accuracy photodiodes (such as those used for self calibration) are discussed in [7]. Current efforts in silicon photodiode modeling aim at high accuracy prediction of the spectral quantum efficiency for the purpose of absolute calibration in radiometry.

Selected numerical results of magnetic field sensor simulations using ALBERTINA are illustrated for unipolar as well as bipolar devices in Figs. 5 to 10. Distributions of carrier transport were computed for a variety of Hall devices under various configurations of discontinuous magnetic induction (Fig. 5). In the case of the Hall cross with a longitudinal strip domain, we observe strips of Hall fields with current flowing parallel to the inversion boundaries, indicating that the distributions effectively resemble the "Hall effect" analytical model. In the other limiting case of the transverse strip domain, we observe no Hall fields but the current lines are skewed by the local Hall angle. In this case, the distributions obey the "carrier deflection" intuitive model. In the general case where the magnetic field is inhomogeneous in both directions, a mixture of both Hall effect and carrier deflection are involved in a complex way on both sides of the inversion boundary. The analysis of such configurations in terms of simple analytical models could become very complicated, if

not impossible. A comparison of experimental and numerical ouput responses is illustrated in Fig. 6, for both bubble and strip domain configurations. As we can see from the figure, the experimental results support the validity of our analysis.

The simulation domain for a bipolar magnetotransistor is shown in Fig. 7 with Fig. 8 illustrating the actual device structure which was fabricated using bipolar technology. The oxide that surrounds the base region (Fig. 7) has been introduced to deal with the problem of boundary conditions discussed in the previous section. To illustrate the effects of magnetic field near the junction vicinity, equipotential lines for the region around the emitter of the device are shown in Fig. 9. The dashed lines indicate the interface between the semiconductor and the oxide at the surface and the bold lines denote the emitter electrode. The device is operated at $V_{BE} = 0.85$ V with a magnetic field of 2 Tesla parallel to the chip surface. The current through the device is 0.6 mA. The equipotential lines appear to be symmetric around the emitter-base junction indicating that there are no significant Hall fields in that vicinity. The distribution of flow lines for minority carriers (electrons) is illustrated in Fig. 10. In contrast to the distribution of potential, the effect of the magnetic field clearly manifests itself in the distribution of current density. There is no indication of any asymmetry in the injected emitter current at the metallurgical emitter-base junction. The numerical results discussed above yield Hall voltages in the order of μV at the emitter-base junction vicinity. This is too small in magnitude to substantiate the validity of the emitter injection modulation model (see [11]). These predictions gathered from simulations are supported by experimental data obtained from *in situ* Hall probe measurements [11]. A systematic comparison of simulations performed for various device structures lead us to conclude that the dominant operating principle in magnetotransistors with linear response is carrier deflection, while possible nonlinearities can be attributed to magnetoconcentration effects.

In mechanical sensor design and development, numerical analysis serves as a valuable tool, reducing the number of redesign cycles [13]. In the design of a silicon cantilever accelerometer (singly fixed beam), the general purpose finite element code ANSYS has been extensively used to predict stress patterns on the beam, the sensitivity, the fundamental as well as higher order resonant modes, temperature coefficient, and overrange characteristics [13]. Knowledge of the stress distribution on the beam aids resistor placement. Results of modal analysis are illustrated in Fig. 11, where the fundamental bending mode is at a resonant frequency of 839 Hz and a second (torsional) resonant mode at 68,575 Hz. Hence, for a given measurement bandwidth, one determines *a priori* whether the higher order modes would present serious problems.

Acknowledgements

REFERENCES

[1]   S. Middelhoek and J. Van der Spiegel (Editors), *State of the Art of Sensor Research and Development*, reprint of *Sensors and Actuators*, **10**, Elsevier Sequoia S. A., Lausanne, 1986.

[2]   H. P. Baltes and R. S. Popovic, "Integrated semiconductor magnetic field sensors," *Proc. IEEE*, **74**, pp. 1107-1132, 1986.

[3]   S. Kataoka (Chairman), Transducers '87, The 4th International Conference on Solid-State Sensors and Actuators, *Technical Digest*, IEE Japan, Tokyo, 1987.

[4]   S. D. Senturia (Guest Editor), Special Issue on Microsensors and Microactuators, *IEEE Trans. Electron Devices*, **35**, pp. 711-808, 1988.

[5]   R. S. Muller (Chairman), IEEE Solid State Sensor and Actuator Workshop, *Technical Digest*, IEEE Catalog Number 88TH0215-4, 1988.

[6]   J. L. Gray, *Two-Dimensional Modeling of Silicon Solar Cells*, Ph.D. dissertation, Purdue University, West Lafayette, USA, 1982.

[7]   J. Geist and H. P. Baltes, "High accuracy modeling of photodiode front-region quantum efficiency," *Appl. Opt.*, submitted.

[8]   A. Nathan, *Carrier Transport in Magnetotransistors*, Ph.D. dissertation, University of Alberta, Edmonton, Canada, 1988.

[9]   A. Nathan, W. Allegretto, H. P. Baltes, and Y. Sugiyama, "Carrier transport in semiconductor magnetic domain detectors," *IEEE Trans. Electron Devices*, **34**, pp. 2077-2085, 1987.

[10]   W. Allegretto, A. Nathan, and H. P. Baltes, "Two-dimensional numerical analysis of silicon bipolar magnetotransistors," *Proc. NASECODE V Conference*, J. J. H. Miller, Ed., Dublin: Boole Press, 1987, pp. 87-92.

[11]   A. Nathan, K. Maenaka, W. Allegretto, H. P. Baltes, and T. Nakamura, "The Hall effect in magnetotransistors," *IEEE Trans. Electron Devices*, in press.

[12]   K. W. Lee and K. D. Wise, " "SENSIM": A simulation program for solid state pressure sensors," *IEEE Trans. Electron Devices*, **29**, pp. 34-41, 1982.

[13]   P. W. Barth, F. Pourahmadi, R. Mayer, J. Poydock, and K. Peterson, "A monolithic silicon accelerometer with integral air damping and overrange protection," *Technical Digest*, IEEE Solid-State Sensor and Actuator Workshop, IEEE Catalog No. 88TH0215-4, pp. 35-38, 1988.

[14]   S. Selberherr, *Analysis and Simulation of Semiconductor Devices*, Vienna: Springer-Verlag, 1984.

[15]   G. C. M. Meijer, "Thermal sensors based on transistors," *Sensors and Actuators*, **10**, pp. 103-125, 1986.

[16]   G. Baccarani, M. Rudan, R. Guerrieri, and P. Ciampolini, "Physical models for numerical device simulation," in *Process and Device Modeling*, W. L. Engl, Ed., Amsterdam: North Holland, pp. 107-158, 1986.

[17]   A. W. van Herwaarden and P. M. Sarro, "Thermal sensors based on the Seebeck effect," *Sensors and Actuators*, **10**, pp. 321-346, 1986.

[18]   M. S. Lundstrom, R. J. Schwartz, and J. L. Gray, "Transport equations for the analysis of heavily doped semiconductor devices," Sol.-St. Electronics, **24**, pp. 195-202, 1981.

[19]   O. Madelung, *Introduction to Solid State Theory*, Berlin: Springer-Verlag, 1978.

[20]   V. Zieren, "Integrated silicon multicollector magnetotransistors," Ph.D. dissertation, Delft University of Technology, Delft, The Netherlands, 1983.

[21]   A. C. Beer, *Galvanomagnetic Effects in Semiconductors*, New York: Academic Press, 1963.

[22]   J. J. Wortman, J. R. Hauser, and R. M. Burger, "Effect of mechanical stress on p-n junction device characteristics," J. Appl. Phys., **35**, pp. 2122-2131, 1964.

574

[23]   B. Puers, L. Reynaert, W. Snoeys, and W. M. C. Sansen, "A new uniaxial accelerometer in silicon based on the piezojunction effect," *IEEE Trans. Electron Devices*, **35**, pp. 764-770, 1988.

[24]   K. W. Lee, *Modeling and Simulation of Solid State Pressure Sensors*, Ph.D. dissertation, University of Michigan, Ann Arbor, USA, 1981.

[25]   W. L. Engl, H. K. Dirks, and B. Meinerzhagen, "Device modeling," *Proc. IEEE*, **71**, pp. 10-33, 1983.

[26]   B. Delauney, "Sur la sphère vide," *Bull. Acad. Science USSR (VII), Classe Sci., Mat. Nat.*, pp. 793-800, 1934.

[27]   B. Joe, "Delauney triangulation meshes in convex polygons," *SIAM J. Sci. Stat. Comput.*, **7**, pp. 514-539, 1986.

[28]   K. Y. K. Chau, *Finite Element Mesh Generation for Semiconductor Device Simulation*, M.Sc. thesis, University of Alberta, Edmonton, Canada, 1988.

[29]   G. Strang and G. F. Fix, *An Analysis of the Finite Element Method*, Englewood Cliffs, New Jersey: Prentice-Hall, 1973.

[30]   I. Babuska and A. K. Aziz, "On the angle condition in the finite element method," *SIAM Journal of Numerical Analysis*, **13**, pp. 214-216. 1976.

[31]   R. E. Bank and D. J. Rose, "Parameter selection for Newton-like methods applicable to nonlinear partial differential equations," *SIAM Journal of Numerical Analysis*, **17**, pp. 806-822, 1980.

[32]   W. Allegretto, A. Nathan, and H. P. Baltes, " Numerical Analysis of magnetic-field-sensitive bipolar devices," *IEEE Computer Aided Design*, submitted.

[33]   D. L. Scharfetter and H. K. Gummel, "Large-signal analysis of a silicon read diode oscillator," *IEEE Trans. Electron Devices*, **16**, pp. 64-77, 1969.

[34]   A. George and J. W. H. Liu, "The design of a user interface for a sparse matrix package," *ACM Trans. on Math Software*, **5**, pp. 139-162, 1979.
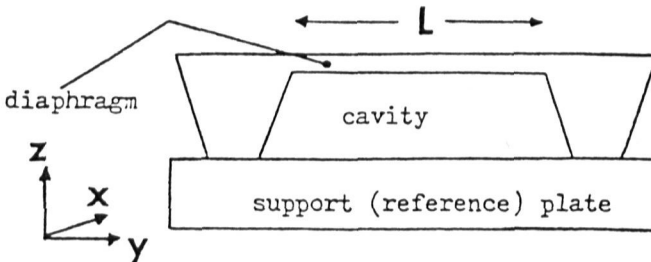
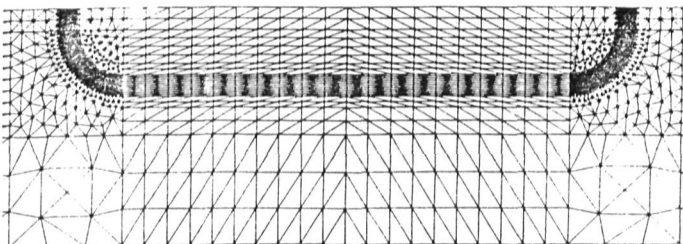Fig. 1.   Cross-sectional view of a pressure transducer

Fig. 2   Triangular mesh for an emitter base junction of a magnetotransistor, generated using Delauney triangulation at junction sidewalls and regular grid triangulation everywhere else [8].
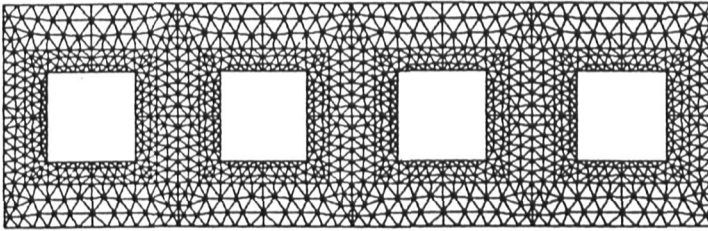
Fig. 3   Delaunay triangulation for a microbridge with apertures
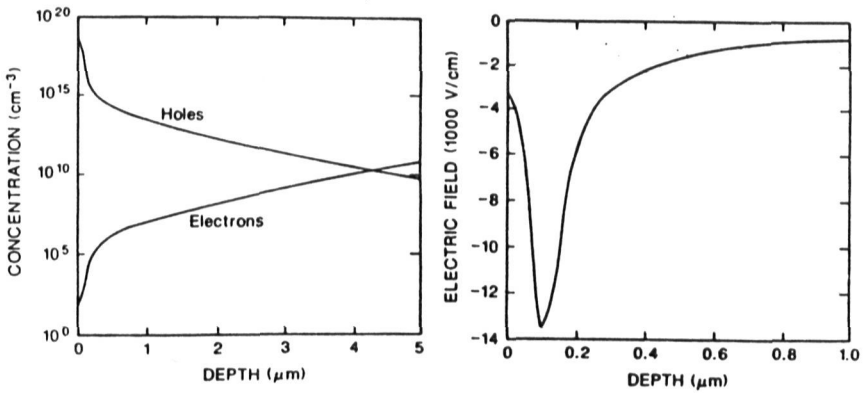   (*Courtesy of Chau* [28]).

Fig. 4   The electric field and carrier concentrations at equilibrium as a function of
          depth. The nominal front region parameters used are characteristic of the
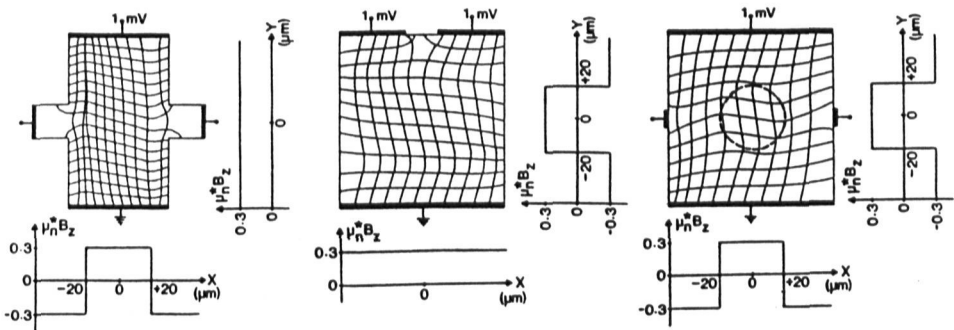   Hamamatsu 1337 photodiode (*Courtesy of Geist* [7]).

Fig. 5   Equipotential and current lines for a Hall cross with longitudinal strip
          domain, a split-electrode Hall device with transverse strip domain, and a
          conventional Hall device with bubble domain [9].
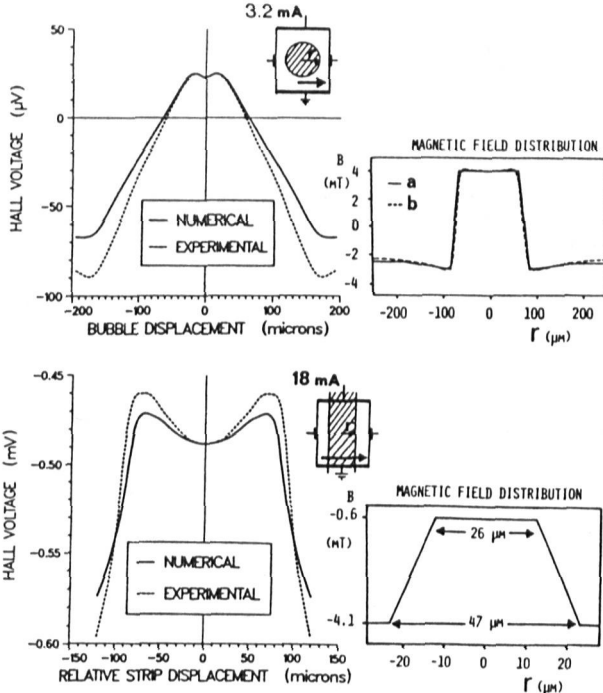
Fig. 6   Comparison of experimental and numerical results of output response for the bubble and strip domain configurations. The bubble distribution used in simulations is denoted by "a" and the measured bubble distribution is denoted by curve "b" [9].
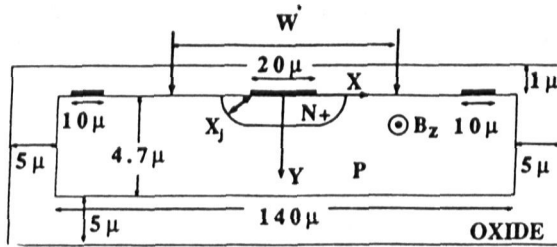

Fig. 7   Two-dimensional simulation geometry of the magnetotransistor's base region surrounded by an artificial oxide region [11].
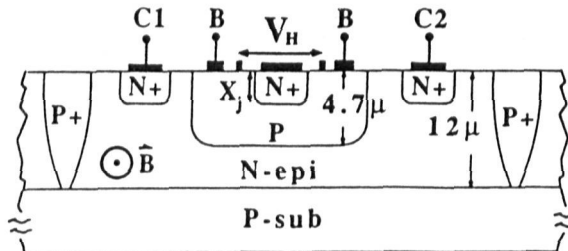

Fig. 8   Cross-sectional view of dual-collector magnetotransistor fabricated in bipolar technology [11].
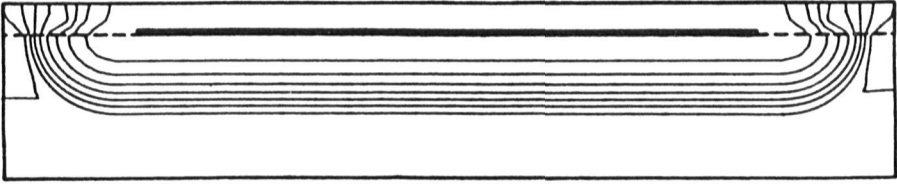
Fig. 9   Equipotential lines the emitter vicinity for $V_{BE} = 0.85$ V and $B = 2$ T [11].
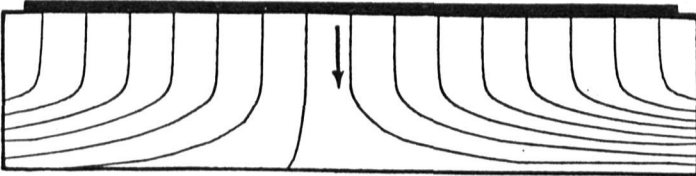

Fig. 10   Minority carrier (electron) flow lines in the vicinity of the emitter for the same operating conditions as in Fig. 9 [11].
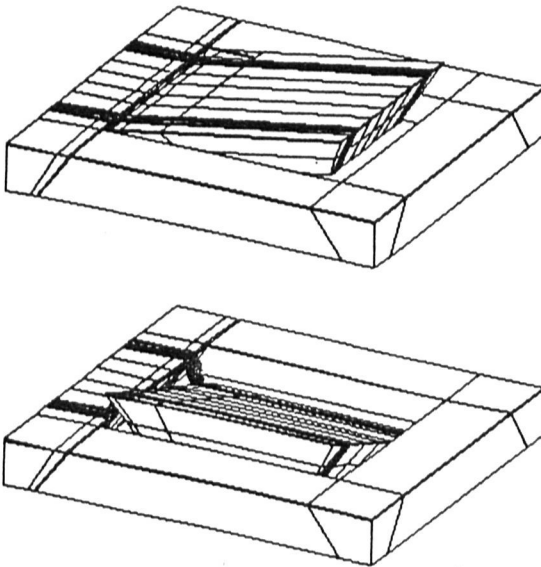

Fig. 11   The fundamental (bending) mode at 839 Hz and second (torsional) mode at 68,575 Hz, for a silicon cantilever accelerometer (*Courtesy of Barth et al.* [13]).